Nanoscale

Transport properties through graphene grain boundaries: strain effects *versus* lattice symmetry

V. Hung Nguyen,*[a,b,c] Trinh X. Hoang,[c] P. Dollfus[b] and J.-C. Charlier[a]

As most materials available at the macroscopic scale, graphene samples usually appear in a polycrystalline form and thus contain grain boundaries. In the present work, the effect of uniaxial strain on the electronic transport properties through graphene grain boundaries is investigated using atomistic simulations. A systematic picture of transport properties with respect to the strain and lattice symmetry of graphene domains on both sides of the boundary is provided. In particular, it is shown that strain engineering can be used to open a finite transport gap in all graphene systems where the two domains are arranged in different orientations. This gap value is found to depend on the strain magnitude, on the strain direction and on the lattice symmetry of graphene domains. By choosing appropriately the strain direction, a large transport gap of a few hundred meV can be achieved when applying a small strain of only a few percents. For a specific class of graphene grain boundary systems, strain engineering can also be used to reduce the scattering on defects and thus to significantly enhance the conductance. With a large strain-induced gap, these graphene heterostructures are proposed to be promising candidates for highly sensitive strain sensors, flexible electronic devices and p–n junctions with non-linear $I-V$ characteristics.

I. Introduction

Graphene-based nanostructures have attracted a great amount of attention from the scientific communities, in view of the numerous possibilities offered not only for fundamental science but also for practical applications.[1] This broad interest is basically motivated by the outstanding properties of graphene such as high carrier mobility, small spin–orbit coupling, superior mechanical strength and stiffness, high electronic and thermal conductivities, optical transparency, *etc*. Hence, graphene appears as a promising material for integration into a variety of electrical, spintronic and optical applications and also for improving the performance of flexible devices.

Regarding the production of a large graphene area, the chemical vapor deposition (CVD) method is known to be the best technique as it is capable of achieving both high structural quality and wafer-scale growth.[2] However, the transfer of graphene to insulating substrates remains a big challenge and considerable efforts are still needed to further improve the

growth process. In particular, CVD graphene is found to be polycrystalline in nature[3,4] and composed of many single-crystal graphene domains separated by grain boundaries (GB) of irregular shapes. The GBs appear as extended structural defects consisting of a random one-dimensional distribution of non-hexagonal rings (*i.e.*, pentagon, heptagon, octagon, *etc.*). These structural defects strongly affect the overall properties of wafer-scale graphene materials.[5] In particular, it has been shown that the intrinsic strength of graphene samples is strongly modified according to the type of grain boundaries.[6–8] Additionally, the grain boundaries are an important source of scattering that limit drastically the carrier mobility in CVD graphene samples[9,10] and consequently the performance of graphene-based electronic devices.[11] The optical and thermal properties of graphene are also significantly affected by the presence of these structural defects.[12–15] The localized states at grain boundaries also play an important role in the transport properties of graphene samples. For instance, strongly localized states at the center of Landau levels and extended electronic states between Landau levels are observed in polycrystalline graphene, which is opposite to that of the conventional quantum Hall effect.[16] Interestingly, such localized states essentially respond to van Hove singularities in the density of states[17] and enhanced magnetism in polycrystalline graphene systems.[18]

Besides its intrinsic defective nature, graphene also exhibits an important drawback: the lack of a bandgap, which is a real problem for conventional applications in electronics.[19] So far,

[a]Institute of Condensed Matter and Nanosciences, Université catholique de Louvain, Chemin des étoiles 8, B-1348 Louvain-la-Neuve, Belgium. E-mail: viet-hung.nguyen@uclouvain.be
[b]Institut d'Electronique Fondamentale, CNRS, Univ. Paris Sud, Université Paris-Saclay, 91405 Orsay, France
[c]Center for Computational Physics, Institute of Physics, Vietnam Academy of Science and Technology, P.O. Box 429 Bo Ho, 10000 Hanoi, Vietnam

many efforts in engineering a bandgap in graphene have been made to solve this issue. For instance, techniques such as cutting 2D graphene sheets into narrow nanoribbons,[20] depositing graphene on a hexagonal boron nitride substrate,[21] doping graphene with nitrogen,[22] applying an electric field perpendicularly to Bernal-stacking bilayer graphene,[23] creating graphene nanomeshes,[24] using hybrid graphene/hexagonal boron-nitride[25] or vertical graphene channels[26] are a few examples. Recently, it has also been suggested that the use of hetero-channels consisting of two graphene domains with different electronic structures could be a potential strategy.[27–29] The idea is that by joining two semi-metallic graphene domains, a finite energy gap of conductance/current through the channel can be achieved if the Dirac cones of these domains are shifted from each other in the k-space. Following this idea, a finite energy gap as large as a few hundred meV has been predicted in unstrained/strained graphene heterojunctions[27] and in vertical channels made of misoriented graphene layers[28] when the strain is conveniently applied. Furthermore, the transport gap has been shown to be strongly dependent not only on the strain magnitude but also on both the strain direction and the lattice orientation. This idea of opening a finite transport gap due to the mismatch between Dirac cones has been also explored in hetero-structures based on the vertical stacking of two different Dirac materials (graphene, silicene, germanene, *etc.*).[30] Given the superior ability to sustain a large strain of over 20%,[31] graphene appears as a promising material for flexible electronic devices.[32] In this regard, the studies in ref. 27 and 28 have suggested a new route to enlarge the possibility of using graphene in strain sensors and flexible transistors. It is worth noting that strain engineering has also been demonstrated to be an alternative/efficient approach to modulate the electrical, optical and magnetic properties of several graphene nanostructures.[33–40]

In polycrystalline graphene, the graphene domains surrounding a grain boundary frequently have different orientations. This naturally offers the possibility of designing heterostructures with similar properties as those studied in ref. 27–29. In principle, a finite transport gap can be achieved in the presence of a mismatch between the band structures of these two graphene domains. Indeed, it has been demonstrated in ref. 41 that a large transport energy gap of about 1 eV can be achieved in a graphene structure made of an incommensurable couple of armchair-oriented and zigzag-oriented domains on both sides of a grain boundary. However, in graphene systems made of two commensurable lattices, the gap remains zero. It has been also shown that the electronic transport through a grain boundary can be modulated by strain engineering.[42] Actually, by applying the strain perpendicularly to the GB, that is the only strain direction investigated in ref. 42, a finite gap can be induced if the two domains of commensurable systems are asymmetric with respect to the GB while the gap in the incommensurate cases can be significantly modified by strain. However, a strain amplitude of about 15–20% appears to be required to achieve a large modulation

of the transport gap and conductance. We would like to emphasize that the requirement of such a large strain is a big challenge in practice. On the one hand, the presence of grain boundaries can severely weaken the intrinsic strength of polycrystalline systems, compared to that of pristine graphene.[43–47] On the other hand, to our knowledge, the highest strain reported that has been attained in a controlled, reversible and reproducible way is just about 10% (see in ref. 48 and references therein). Besides this limitation, a strain applied perpendicularly to the GB as in ref. 42 cannot change the semi-metallic character of symmetric systems. As suggested in similar graphene heterosystems,[27,28] the transport gap should strongly depend not only on the strain magnitude but also on the strain direction. Hence, the strain direction studied in ref. 42 may not be the optimal one to achieve a large gap and hence cannot fully clarify the high strain-sensitivity of the charge transport in these kinds of heterostructures. In addition, since the transport gap is essentially due to the mismatch between the electronic structures of two graphene domains, we anticipate that the symmetry properties of the global system should play an important role, which has not been properly investigated yet.

In this context, we aim to investigate systematically the effects of uniaxial strain on the transport properties of graphene-based systems containing a single grain boundary. First, we clarify systematically the dependence of the transport gap on (i) the strain (both in amplitude and applied direction) and (ii) the symmetry properties of the global system that are characterized by the nature of the grain boundary, both orientations of the two graphene domains, their relative commensurability, and so on. Based on this, we explore the possibilities of strongly modulating/generating a transport gap in all systems where the graphene domains have different orientations and, especially, for small strain amplitudes of only a few percents. We also report on a new property of scattering on defects in graphene grain boundary systems when a strain is applied. Finally, we suggest some typical applications of these kinds of graphene heterostructures and study in more detail the case of p–n junctions exhibiting strong negative differential conductance and rectification effects.

II. Model and methodology

The investigated graphene-based systems containing a single grain boundary that presents periodic pentagon–heptagon pairs along the Oy direction are illustrated as in Fig. 1. In this work, we consider the electronic transport along the Ox direction, *i.e.*, perpendicularly to the grain boundary.[49,50] A uniaxial strain applied to the system is characterized by its magnitude ε and its direction θ with respect to the transport direction (see the inset on the right of Fig. 1).

In most cases, graphene domains surrounding the boundary exhibit different crystallographic orientations. More specifically, we distinguish two typical cases for these domains depending on their lattice relative symmetries (see Fig. 1).
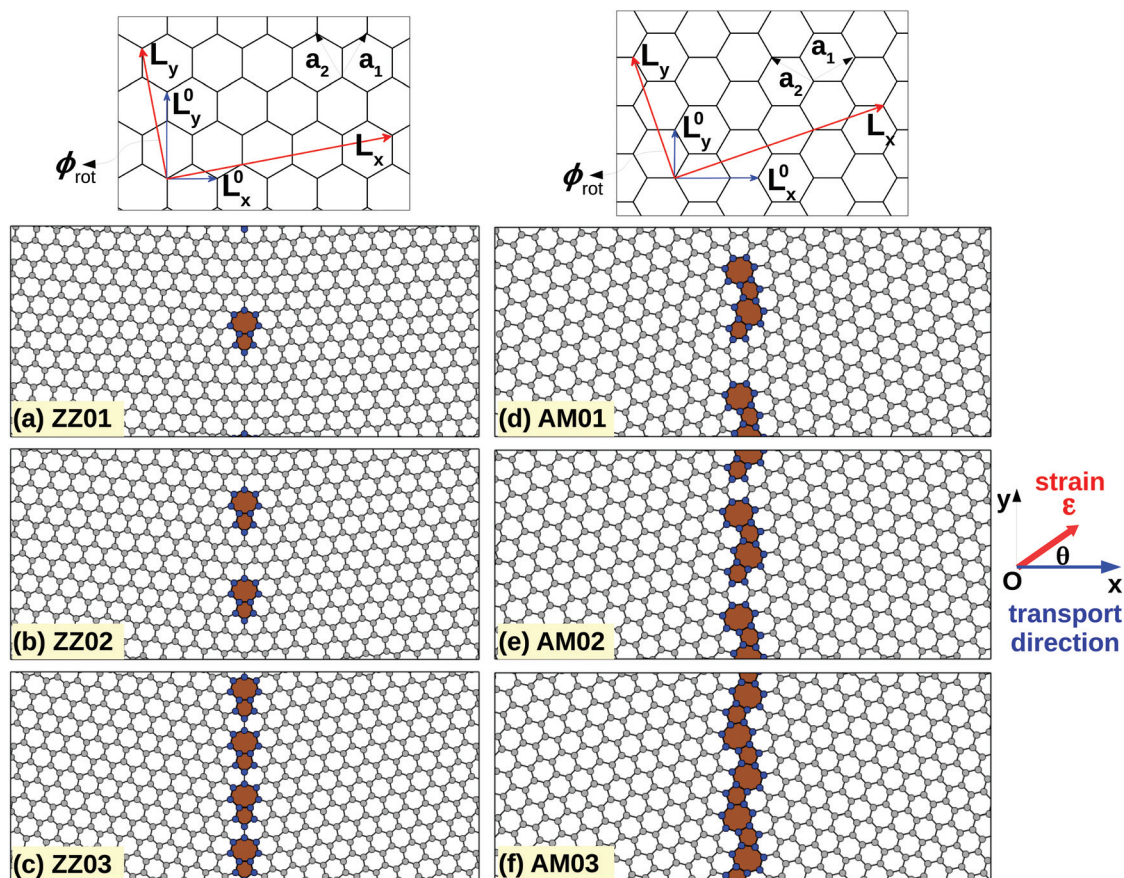
Fig. 1 Graphene-based systems investigated in this work. The systems contain a single grain boundary that presents periodic pentagon–heptagon pairs along the Oy axis. The top images illustrate the rotation of the graphene sheet to form two graphene domains surrounding the grain boundary (see text). The transport direction (Ox axis) is perpendicular to the grain boundary. The uniaxial strain of magnitude ε is applied in the direction θ with respect to the Ox axis as illustrated by the small inset on the right side.

In both cases, the domains are determined by rotating the original (zigzag- or armchair-oriented) lattice by an angle ϕ_{rot}. This angle is actually the angle between translation vectors $\vec{L}_y$ of the rotated lattice and $\vec{L}_y{}^0$ of the original one (see the images in the top of Fig. 1) and determined as $\cos \phi_{\mathrm{rot}} = \dfrac{\vec{L}_y \cdot \vec{L}_y{}^0}{L_y L_y{}^0}$. These vectors are simply given by $\vec{L}_y{}^0 = \vec{a}_1 + \vec{a}_2$ while $\vec{L}_y = p\vec{a}_1 + q\vec{a}_2$. Before the rotation, $\vec{a}_{1,2} = (\pm\sqrt{3}, 3)a_0/2$ and $(\pm 3, \sqrt{3})a_0/2$ in the zigzag- and armchair-oriented lattices, respectively, where a_0 is the in-plane C–C bond length (= 1.42 Å) in pristine graphene. Hereafter, these zigzag- and armchair-oriented lattices are identified with the denominations $ZZ_{p,q}$ and $AM_{p,q}$, respectively. Accordingly, we also determine the translational vectors along the Ox axis as $\vec{L}_x = n\vec{a}_1 + m\vec{a}_2$ that satisfies the condition $\vec{L}_x \cdot \vec{L}_y = 0$, i.e., $\dfrac{n}{m} = -\dfrac{2q+p}{2p+q}$ for $ZZ_{p,q}$ and $\dfrac{n}{m} = -\dfrac{2q-p}{2p-q}$ for $AM_{p,q}$ lattices. Depending on their orientation and the periodicity of the grain boundary, the supercell of graphene domains can be classified into two cases where either $L_x = L_y\sqrt{3}$ if $p - q \neq 3l$ (supercell of type 1) or $L_x = L_y/\sqrt{3}$ if $p - q = 3l$ (super-

cell of type 2) with $l \in \mathbb{Z}$ [41] for $ZZ_{p,q}$ lattices. For $AM_{p,q}$ ones, we have $L_x = L_y\sqrt{3}$ if $p + q \neq 3l$ and $L_x = L_y/\sqrt{3}$ if $p + q = 3l$. We also distinguish two types of grain boundary systems where the left and right graphene domains are either commensurable or incommensurable. In the commensurable cases, one can find a common periodicity for the two graphene domains by extending the supercell appropriately from the original lattices, which is not the case for the incommensurable lattices. Hence, the translational length L_y is exactly the same for both domains in the commensurable systems while there is a mismatch between their translational lengths in the incommensurable cases. Regarding the incommensurable systems studied in the present work, we only focus on the cases where the mismatch mentioned above is small (i.e., ≲3%), which allowed us to perform calculations using the average translational length as the size for the periodic cells along the Oy axis.[41]

Each graphene-based system was relaxed using classical molecular dynamics to minimize its energy determined from optimized Tersoff potentials.[51] This empirical potential model has been shown to accurately describe the structural properties

and to provide accurate calculations of the thermal/mechanical properties in pristine and defective graphene including grain boundaries.[14,15,52–57] To compute the electronic transport quantities, we then employed a non-equilibrium Green's function formalism to solve the π-orbital tight-binding model. It is worth noting that the agreement between tight-binding calculation and density functional theory in graphene GBs has been demonstrated in ref. 41. It has to be also noted that even without applying any external strain, local strains caused by the atomic dislocation still occur in the vicinity of the GB. However, while the quantitative value of transmission across the boundary is slightly affected, its qualitative behavior around the gap as well as the transport gap is not significantly affected by this local strain. This can be explained by the fact that the transport gap is essentially due to the mismatch between electronic structures of graphene lattices in both sides (far from the grain boundary) where the effects of atomic dislocations are negligible.

In particular, the real space tight-binding Hamiltonian was constructed as follows: $H_{tb} = \sum_{i,j} t_{i,j} c_i^+ c_j$ where $t_{i,j}$ corresponds to the nearest-neighbor hopping energy between i^{th} and j^{th} atoms. When a uniaxial strain is applied, the change in the C–C bond vectors $\vec{r}_{ij}$ was determined according to $\vec{r}_{ij}(\vec{\varepsilon}) = \{1 + M_s(\vec{\varepsilon})\}\vec{r}_{ij}(0)$ with the following strain tensor[33]

$$M_s(\vec{\varepsilon}) = \varepsilon \begin{bmatrix} \cos^2\theta - \gamma\sin^2\theta & (1+\gamma)\sin\theta\cos\theta \\ (1+\gamma)\sin\theta\cos\theta & \sin^2\theta - \gamma\cos^2\theta \end{bmatrix} \quad (1)$$

where $\vec{\varepsilon} \equiv (\varepsilon, \theta)$ represents the strain (see in Fig. 1) and $\gamma \simeq 0.165$ is the Poisson ratio.[58] When taking into account strain effects, the hopping parameters were adjusted accordingly,[33] i.e., $t_{ij}(\vec{\varepsilon}) = t_{ij}(0)\exp\left[-3.37\{r_{ij}(\vec{\varepsilon})/a_0 - 1\}\right]$ where $t_{ij}(0) \equiv -2.7$ eV corresponds to the hopping energy between nearest neighbor atoms in pristine graphene. The tight-binding Hamiltonian H_{tb} can be rewritten in its wavevector k_y-dependent (quasi-1D) form $H_{tb}(k_y)$, as described in more detail in ref. 27 and 28. The Green's function was then computed[59] using the equation:

$$\mathcal{G}(E, k_y) = [E + i0^+ - H_{tb}(k_y) - \Sigma(\varepsilon, k_y)]^{-1}, \quad (2)$$

where the self-energy $\Sigma(E, k_y) = \Sigma_L(E, k_y) + \Sigma_R(E, k_y)$ with $\Sigma_{L,R}$ being the terms that describe the left and right contact-to-device couplings, respectively. The transmission probability needed to evaluate the current is calculated as $\mathcal{T}_e(E, k_y) = \text{Tr}\{\Gamma_L \mathcal{G} \Gamma_R \mathcal{G}^\dagger\}$, with $\Gamma_{L(R)} = i(\Sigma_{L(R)} - \Sigma_{L(R)}^\dagger)$ being the transfer rate at the left (right) contact. The conductance and current were obtained by the Landauer formulas:

$$G = \frac{e^2 W}{\pi h} \int_{BZ} dk_y \int dE \mathcal{T}_e(E, k_y) \left\{ -\frac{\partial f(E)}{\partial E} \right\}, \quad (3)$$

$$I = \frac{eW}{\pi h} \int_{BZ} dk_y \int dE \mathcal{T}_e(E, k_y) \{f_L(E) - f_R(E)\}. \quad (4)$$

Here, the integrals over k_y are performed in the whole Brillouin zone, W denotes the channel width, and $f_{L(R)} = 1/[1 + \exp$ $((E - E_{FL(R)})/k_b T)]$ is the Fermi distribution function in the left (right) contact with the Fermi energy level $E_{FL(R)}$.

III. Results and discussion

Within the methodology described above, we investigate the transport properties through different graphene grain boundary systems.

A. Transport gap induced by strain

First, we investigate the transport properties of the symmetrical graphene-based systems schematized in Fig. 1. Considering a strain applied along the Ox axis, the symmetrical graphene GBs have been found to always remain semi-metallic.[42] However, this conclusion is no longer true when the strain direction is changed. The strain effects on the transmission function obtained in the system with the $ZZ_{2,1}$ and $ZZ_{1,2}$ lattices surrounding the GB (see Fig. 1c) are represented in Fig. 2. It is true that in the unstrained case and for a strain $(\varepsilon,\theta) = (4\%, 0°)$, the system remains semi-metallic with a zero energy gap in its transmission function. However, when the strain direction is changed, a significant gap E_g opens, as shown in Fig. 2c and d. The origin of this feature can be easily explained as follows. Since the two graphene domains are arranged in different orientations, the effects of strain on their electronic structures are generally different. In particular, their band structures are identical in the commensurable system studied here (see the band-edges superimposed in Fig. 2a) when no strain is applied. However, when a strain is applied in an appropriate direction, their band structures are deformed differently, leading to a separation of their Dirac cones along the k_y axis (see the band-edges superimposed in Fig. 2c and d). This separation results in a finite energy interval where there is no overlap between the band structures of the two domains. In the presence of a periodic grain boundary, the charge transport through the system satisfies the k_y conservation and hence only the states in the overlapped region of band structures can be transmitted. Otherwise, a gap of transmission, i.e., a transport gap, is formed. Essentially, this transport is proportional to the separation between the Dirac cones of the two domains $\Delta D_y = |D_{1y} - D_{2y}|$, i.e., $E_g \simeq \hbar v_F \Delta D_y$ with the Fermi velocity $v_F = 10^6$ m s^{-1}. Note that the same separation is obtained for the D' cones, i.e., $\Delta D'_y = |D'_{1y} - D'_{2y}| \equiv \Delta D_y$. This property explains why the structure is gapless (i.e., $\Delta D_y = 0$) when no strain is applied, as shown in Fig. 2a. Because of the system symmetry with respect to the grain boundary, ΔD_y (and E_g) remains zero when a strain is applied along the Ox direction ($\theta = 0°$). For other strain directions, in particular $\theta = 20°$ and $45°$ presented in Fig. 2c and d, the system symmetry mentioned is broken by strain and hence a finite ΔD_y (and E_g) is achieved.

In Fig. 3, maps of the transport gap with respect to the strain magnitude (from 0% to 6%) and its applied direction were calculated for the different graphene systems described in Fig. 1. Except for the AM02 case that will be discussed later,
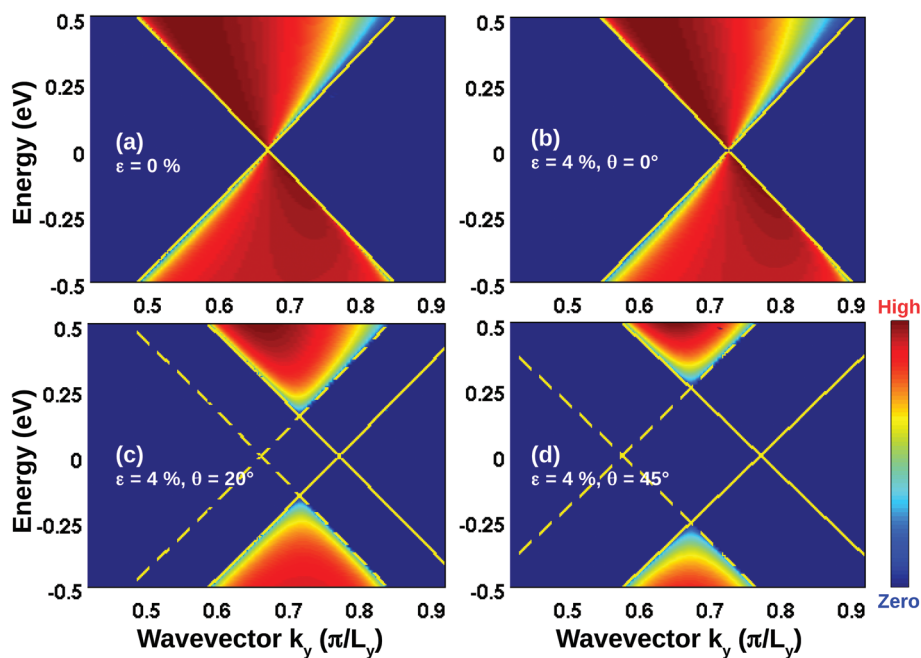
Fig. 2 Transmission probability maps around the neutrality (Dirac) point obtained in the graphene GB system ZZ03 (see Fig. 1c). Various applied strains (ε,θ) are considered. The dashed and solid lines are superimposed to show the strain effects on the band (conduction and valence) edges of the two graphene domains along the k_y axis.
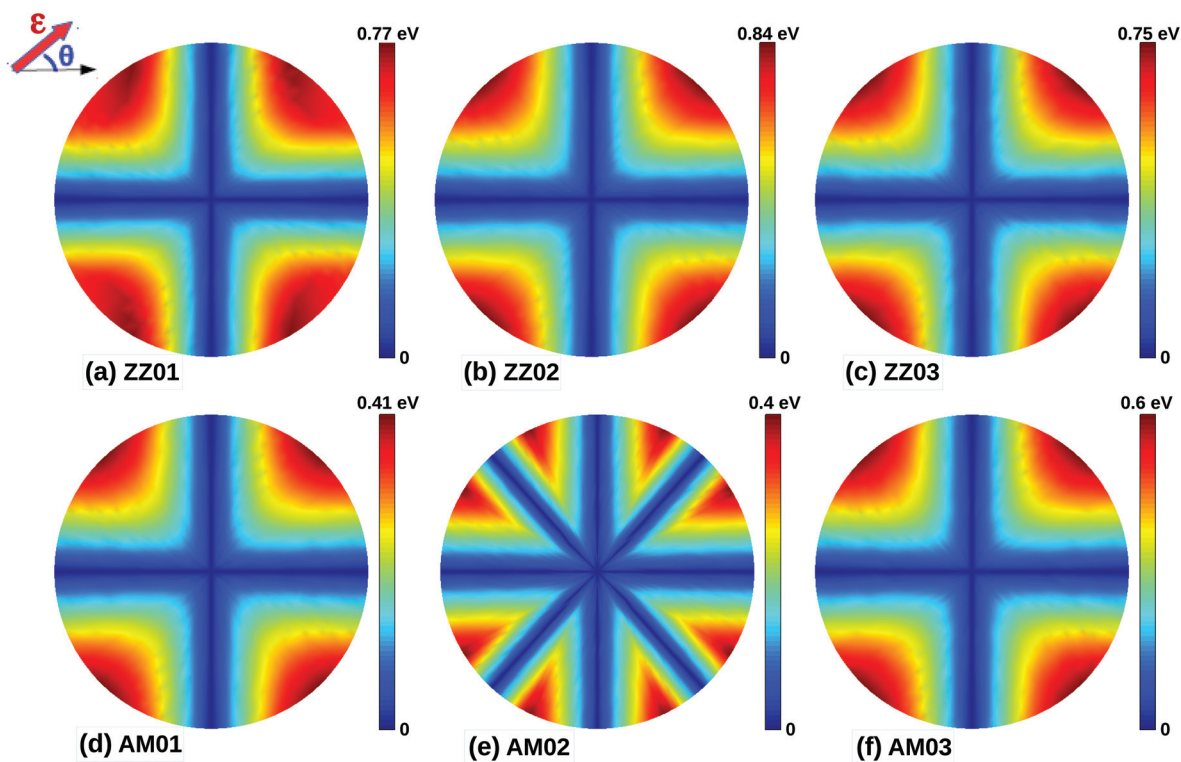

Fig. 3 Color maps of the transport-gap with respect to the strain (ε,θ) in different graphene GB systems (see Fig. 1). Note that the radius from the central point of the maps represents the strain magnitude ranging from 0% (center) to 6% (edge).

the transport gap is zero for $\theta = i \times 90°$ (where i = 0, 1, 2, 3) while it gets maximum around $\theta = i \times 90° + 45°$. In conclusion, opening a finite transport gap in graphene GB systems is always possible even if they are symmetric. The gap value is strongly dependent on both the strain magnitude and its applied direction. Interestingly, when strain is applied in the appropriate direction, a large transport gap of a few hundred meV can be achieved with the strain magnitude as small as a few percents. For instance, a large gap of ~840 meV is achieved for ε = 6% as shown in Fig. 3b.

Moreover, Fig. 3 also demonstrates that besides its dependence on the strain magnitude and strain direction, the transport gap is also very sensitive to the system symmetry. First, as explained above, the key factor responding to the strain-induced generation/modulation of the transport gap in these kinds of graphene heterostructures is the degree of misorientation between the two domains. The transport gap cannot be neither created nor modulated in the systems consisting of the same oriented graphene lattices (e.g., graphene sheet with a line defect[60]) because a mismatch between their electronic structures does not occur even if a strain is applied. Therefore, the transport gap is generally dependent on the misorientation angle ϕ_{MO} between the two graphene domains. Indeed, for zigzag-oriented lattices and for small strains, the gap generally decreases when increasing the misorientation angle as shown for instance in the cases ZZ02 ($\phi_{MO} \approx 13.2°$) – Fig. 3b and ZZ03 ($\phi_{MO} \approx 21.8°$) – Fig. 3c. However, for armchair-oriented lattices, the gap has an opposite behavior, which is seen in the cases AM01 ($\phi_{MO} \approx 17.9°$) – Fig. 3d and AM03 ($\phi_{MO} \approx 27.8°$) – Fig. 3f. Here, we would like to notice that the band structure of graphene domains surrounding the grain boundary is actually obtained by band folding from the original lattice. In principle, the resulting band folding is essentially dependent on both the rotation of the graphene sheet and its original lattice. In the original lattices, the Dirac cones are located at different positions in the k-space, i.e., at $\left(\mp \dfrac{2\pi}{3L_x}, 0 \right)$ and $\left(0, \mp \dfrac{2\pi}{3L_y} \right)$ in the zigzag- and armchair oriented cases, respectively. Hence, the folded bands of the corresponding rotated lattices have different behaviors under the effect of strain, which can explain the results discussed above regarding the ϕ_{MO}-dependence of E_g. Moreover, since the system symmetry is dependent not only on the orientation of two graphene domains but also on the nature of the grain boundary (e.g., its direction, periodic length L_y, etc.), it will be shown later (see the discussions for Fig. 8 and 9 below) that besides its dependence on the misorientation angle, the transport gap also exhibits a strong sensitivity to other structure parameters.

Next, the behavior of the transport gap is found to be strongly dependent on the supercell (type and size) of graphene domains. In Fig. 4a, the transport gap is presented as a function of strain direction θ for ε = 6% in the armchair-oriented cases. Actually, the transport gap in the AM02 system ($\phi_{MO} \approx 21.8°$) obtained for strain directions close to $\theta = i \times 90°$ also satisfies the ϕ_{MO}-dependence discussed above for the armchair-oriented systems. However, in contrast with the other cases, it exhibits an additional valley, instead of a maximum, around $\theta = i \times 90° + 45°$ (see also Fig. 3e). To explain this feature, the supercell and Brillouin zone of two typical graphene lattices are illustrated in Fig. 4b and c. The displacement of the Dirac cones when changing the strain direction is also depicted. As mentioned, the supercell of graphene lattices has two possible types, i.e., either $L_x = L_y \sqrt{3}$ (type 1) or $L_x = L_y / \sqrt{3}$ (type 2). These supercell types correspond to the two cases where $p - q \neq 3l$ ($p + q \neq 3l$) and $p - q = 3l$ ($p + q = 3l$), respectively, for $ZZ_{p,q}$ ($AM_{p,q}$) systems as described in the previous section. Accordingly, there are two different types of Brillouin zones and the corresponding Dirac points (i.e., at the K-points without strain) are located either at
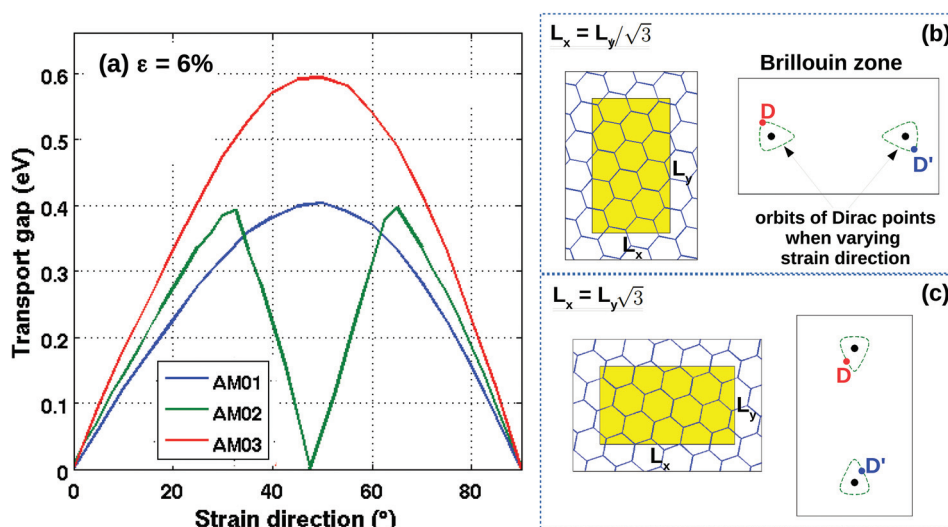

Fig. 4 Transport gap *versus* strain direction θ in armchair oriented graphene based systems for ε = 6% (a). Two supercell types (see text) and corresponding Brillouin zones of the rotated graphene lattices are illustrated in (b) and (c).

$\left(\mp\dfrac{2\pi}{3L_x},0\right)$ or at $\left(0,\mp\dfrac{2\pi}{3L_y}\right)$, respectively (see Fig. 4b and c). In the AM01, AM03, ZZ01, ZZ02 and ZZ03 systems (*i.e.*, $L_x = L_y\sqrt{3}$), the transport gap E_g is simply proportional to $\Delta D_y = |D_{1y} - D_{2y}|(\equiv |D'_{1y} - D'_{2y}|)$. Hence, E_g represents a maximum around $\theta \approx i \times 90° + 45°$ while it is zero for $\theta = i \times 90°$ when $D_{1y} \equiv D_{2y}$ and $D'_{1y} \equiv D'_{2y}$. However, the situation is different for the AM02 systems (*i.e.*, $L_x = L_y/\sqrt{3}$) since ΔD_y is the minimum of $|D_{1y} - D_{2y}|$, $|D_{1y} - D'_{2y}|$, $|D'_{1y} - D_{2y}|$ and $|D'_{1y} - D'_{2y}|$, making twice smaller the period of θ-values for which the transport gap vanishes. Hence, besides the zero value of E_g at $\theta = i \times 90°$, the gap is also zero with a corresponding valley around additional points $\theta \approx i \times 90° + 45°$ when $|D_{1y} - D'_{2y}|$ $(\equiv |D'_{1y} - D_{2y}|)$ is zero or small. Note that this dependence of E_g on the supercell type is a common property for all graphene GB systems even if (not shown in this paper) graphene domains are asymmetric (but still commensurable) or incommensurable.

In order to investigate its dependence on the supercell size, the transport gap is plotted as a function of strain direction θ in Fig. 5a and of strain magnitude in Fig. 5b for the cases of zigzag-oriented systems. Note that the transport gap in the

ZZ01 system ($\phi_{MO} \approx 9.4°$) obtained for small strains or large strains with directions close to $\theta = i \times 90°$ also satisfies the ϕ_{MO}-dependence discussed above for the zigzag-oriented systems (see Fig. 5a). However, when the strain magnitude is large enough, the gap around $\theta = 45°$ obtained in this system is suddenly reduced when increasing ε. To clarify this feature, the transport gap is investigated in a large range of ε while θ is fixed at 45° (Fig. 5b). Actually, in all cases, the gap is found to increase with the strain magnitude and then to decrease when ε is large enough. The gap can even vanish at $\varepsilon \simeq 14.3\%$ in the case of the ZZ01 system (Fig. 5b). Interestingly, the threshold value of strain ε_{peak} at which the behavior of E_g changes is found to be inversely proportional to the size L_y of the super-cell. In particular, ε_{peak} is ~11.2%, 6.7% and 4.9% for $L_y \simeq$ 0.65 nm (ZZ03), 1.1 nm (ZZ02) and 1.5 nm (ZZ01), respectively. To explain these properties, we draw in Fig. 5c some diagrams illustrating visually the displacement of the Dirac cones of both graphene domains along the k_y axis when a large strain is applied. For small strains, the Dirac cones D_1 (of domain 1) and D_2 (of domain 2) are gradually separated, which makes the transport gap increase with the strain magnitude. When the strain is large enough, D_1 reaches the edge of the Brillouin zone and then the situation (1) illustrated in Fig. 5c takes
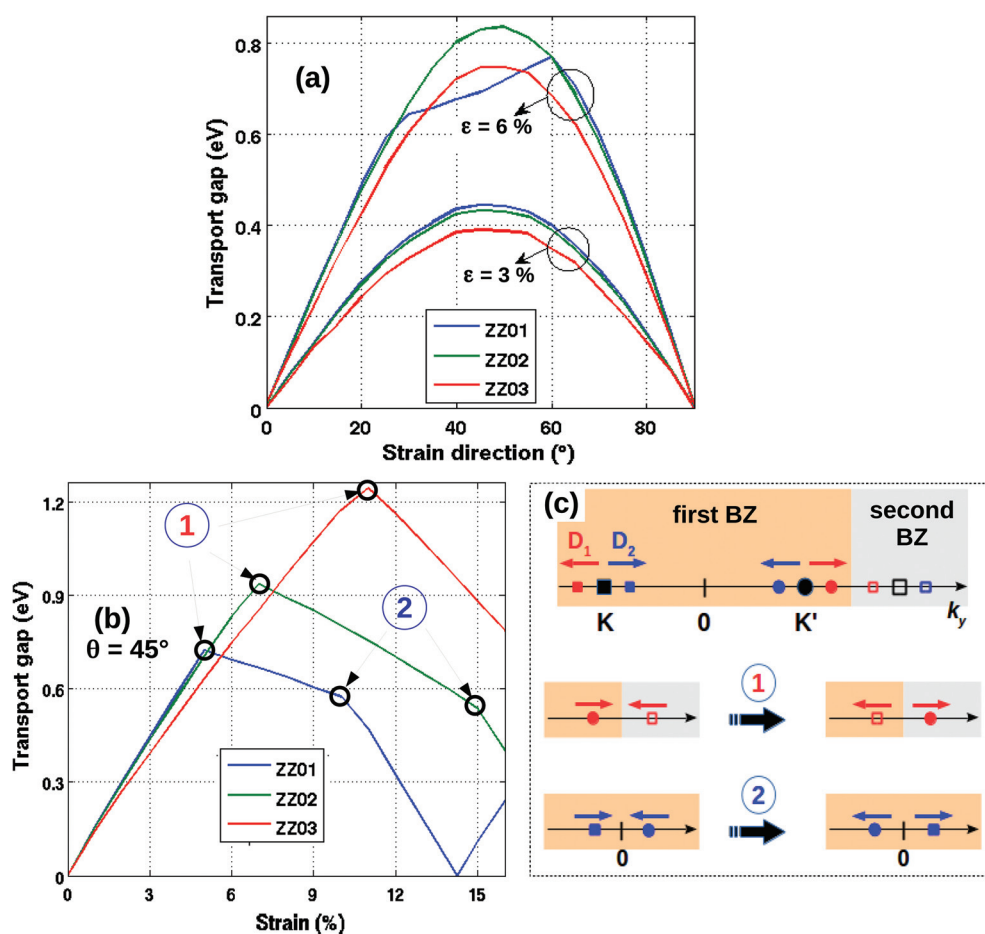

Fig. 5 Transport gap *versus* strain direction θ for two different ε values (a) and *versus* ε for $\theta = 45°$ (b) for zigzag oriented-graphene systems. (c) Schematics illustrating the displacement induced by strain along the k_y axis of the Dirac points related to the two graphene domains (see text).

place, thus modifying the behavior of ΔD_y (and E_g) from an increasing to decreasing function of ε. On further increasing the strain, D_2 reaches the zero point, which induces the situation (2) to happen and makes the gap decrease even more rapidly. Additionally, the dependence of ε_{peak} on L_y is a direct consequence of the L_y-dependence of the size of the Brillouin zone (see further discussions below). For a smaller L_y, the corresponding Brillouin zone is larger and hence the situations described above occur at a larger strain.

We would like to notice that such a merging of Dirac cones when a large uniaxial strain is applied in pristine graphene has already been reported in ref. 33 showing that beyond the critical strain (~23%), a bandgap opens. However, the merging process in the present case is completely different. Indeed, it appears at a much lower strain than the critical value mentioned above and the band structure of graphene domains is still gapless. This is because the presence of a grain boundary changes the periodicity of graphene lattices and the merging process observed here is essentially a consequence of the folding of the graphene band structure from the original Brillouin zone to the reduced Brillouin zone. Actually, the reduced Brillouin zone along the k_y axis is determined as $k_y \in \left[-\dfrac{\pi}{L_y}, \dfrac{\pi}{L_y}\right]$ and hence the maximum of ΔD_y is π/L_y (approximately, the maximum of transport gap is $E_{gmax} = \hbar v_F \pi / L_y$) obtained when, for instance, $D_{1y} = 0$ and $D_{2y} = \pi/L_y$. Generally, it is difficult to simultaneously satisfy these conditions for $D_{1y,2y}$ and hence the maximum of the transport gap, depending on the system symmetry, is always smaller than E_{gmax}. Importantly, the mentioned property suggests that the graphene GB systems with a short periodic length L_y are preferable to obtain a large transport gap induced by strain.

In order to present a general view, the properties of E_g in asymmetrical (but still commensurable) systems have also been investigated. Since the gap is dependent on both the strain and orientation of graphene domains, the properties of E_g should change dramatically when the global system is no longer symmetric. In Fig. 6b, a polar map of E_g with respect to the strain was calculated for the asymmetrical system represented in Fig. 6a. Note that E_g has properties similar to that of symmetrical systems, except that it exhibits a different θ-dependence. In particular, the gap is strongly dependent on the strain direction with valleys of minimal values at $\theta \simeq i \times 90° + 61°$ and high peaks of maximal values in between such valleys. A large gap up to 730 meV for a strain $\simeq$6% is also observed.

The next section is devoted to the effects of strain on the transport gap in incommensurable graphene-based systems. Note that in the incommensurable systems where the two graphene domains have the same supercell type (not shown in this paper), the transport gap has properties similar to that of commensurable ones discussed above. However, differently from the commensurable systems, it is possible to design heterostructures where the graphene domains have different supercell types (see Fig. 4b and c) in the incommensurable cases. In these heterostructures, the Dirac cones of the two graphene domains are located at different positions in the k-space (i.e., at $\left(\mp\dfrac{2\pi}{3L_x}, 0\right)$ and $\left(0, \mp\dfrac{2\pi}{3L_y}\right)$). Consequently, a finite transport gap can be achieved even if no strain is applied.[41] In Fig. 7, the maps of E_g with respect to the strain are displayed for two different incommensurable systems shown in Fig. 7a (INC01) and Fig. 7d (INC02), respectively. Here, both the tensile (Fig. 7b and e) and compressive strains (Fig. 7c and f) are investigated. When no strain is applied, the gaps of ~1 eV and 0.58 eV are obtained for the INC01 ($L_y \simeq 1.23$ nm) and INC02 ($L_y \simeq 2.13$ nm) systems, respectively. Similarly as discussed above, these values of the transport gap approximately satisfy the formula $E_g(0) = 2\hbar v_F \pi / 3L_y$. More interestingly, strain engineering is found to be a very efficient way to modulate the gap. Depending on the strain direction, gaps in the range of [0.31, 1.20] eV and [0.37, 1.38] eV can be respectively achieved when the tensile and compressive strains ($\leq$6%) are applied to the INC01 system. In the case of INC02, the ranges of E_g are [0.0, 0.86] eV (tensile strain) and [0.0, 0.98] eV (compressive strain). Again, the θ-dependence of E_g is shown to be strongly
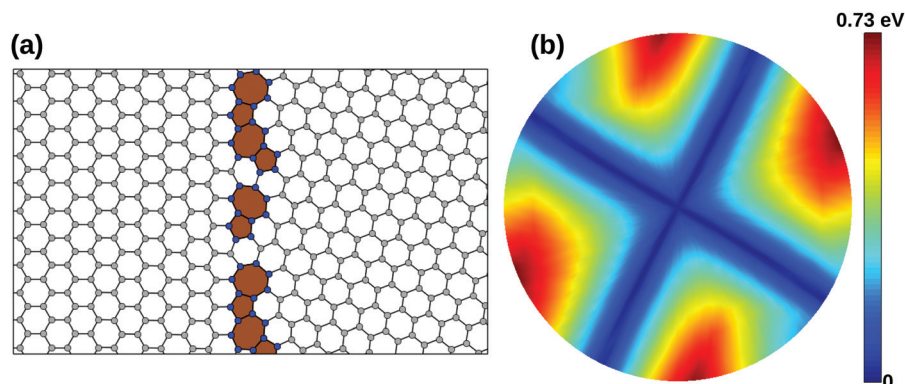

Fig. 6 (a) Asymmetrical graphene GB system: an armchair oriented lattice (on the left) connected to a $ZZ_{3,5}$ lattice (on the right). (b) Color map of the transport gap with respect to the strain (ε,θ). The radius from the central point represents the strain magnitude ε ranging from 0% (center) to 6% (edge).
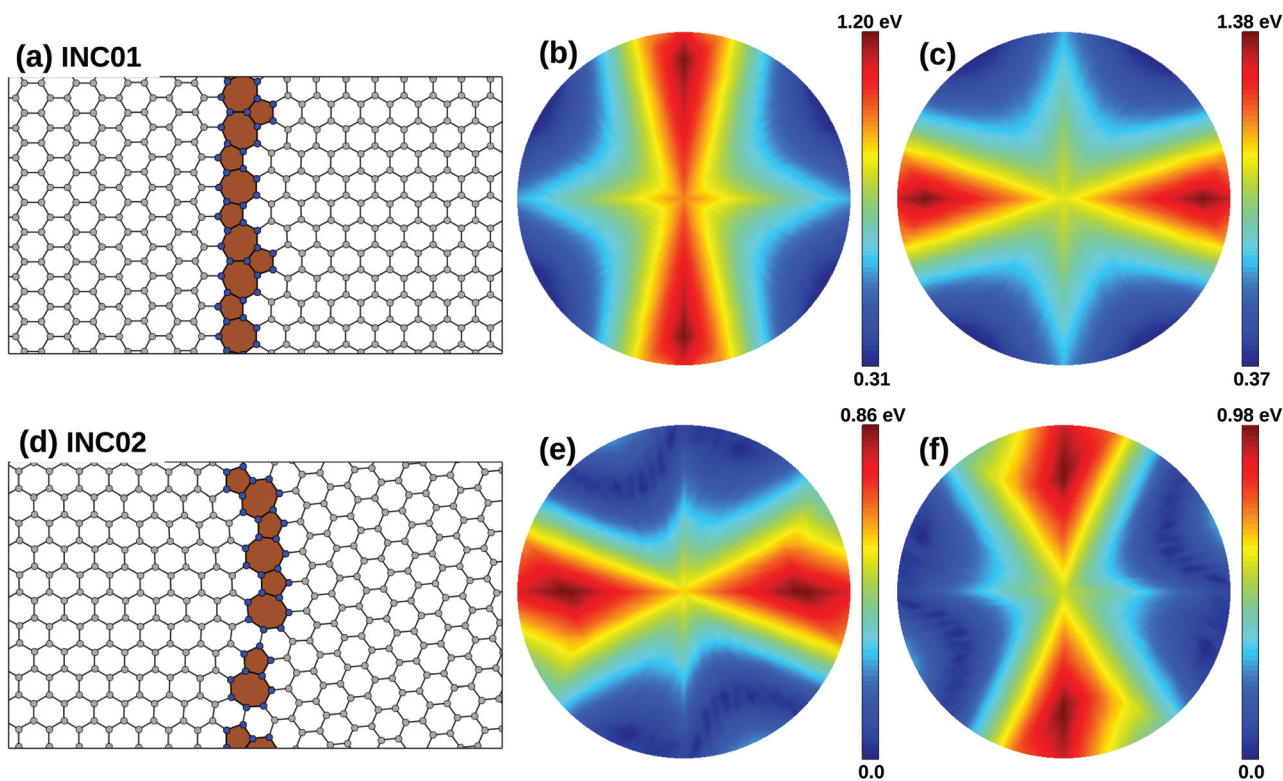
Fig. 7 Color maps (b, c) and (e, f) of the transport gap with respect to the strain (ε,θ) in two incommensurable systems shown in (a) and (d), respectively. Both tensile and compressive strains are considered in (b, e) and (c, f), respectively. The radius from the central point represents the strain magnitude ε ranging from 0% (center) to 6% (edge).

sensitive to the overall symmetry of the system, *i.e.*, it is very different in the INC01 and INC02 cases. Interestingly, even if a finite transport gap is achieved without a strain, a metal–semiconductor transition can be observed for the system INC02 with the strain magnitude $\varepsilon < 6\%$. For the system INC01, such a transition also occurs for a strain of about 8.7% (not shown). In these systems, the maximum of the transport gap when a strain is applied is generally larger than the value $E_g(0)$ but smaller than the value E_{gmax} ($\simeq \hbar v_F \pi / L_y$), as already explained above. Additionally, the behavior of E_g is qualitatively similar in the two strain cases (ε,θ) and $(-\varepsilon,\theta + 90°)$. This can be explained by analyzing the strain tensor in eqn (1). For small strains, the relationship between the bond lengths under these two strains is approximately given by

$$r(\varepsilon,\theta) - r(-\varepsilon, \theta + 90°) \simeq \varepsilon(1 - \gamma)r_0, \qquad (5)$$

which is θ-independent for all C–C bond vectors. It also implies that there is a fixed ratio between the hopping energies $t_{ij}(\varepsilon,\theta)$ and $t_{ij}(-\varepsilon,\theta + 90°)$ and hence the displacement of Dirac cones (and E_g) is qualitatively similar in these two cases.[27] This property is actually valid for all systems, *i.e.*, also including the commensurable cases studied above. The only difference between the effects of the two types of strain is that the

gap varies more strongly under a compressive strain than under a tensile one.

For the sake of completeness, we present in Fig. 8 the strain-induced transport gap obtained in some systems[61] where the grain boundary (direction and/or periodic length L_y) is modified. The two graphene domains in Fig. 8a–c are the same as in Fig. 1c while the domains in Fig. 8d and e are the same as in Fig. 7a. As emphasized above, the symmetry property of the global system is dependent on both the orientation of the two domains and on the nature of the grain boundary. Indeed, Fig. 8 shows that the degree of symmetry between two domains, their relative orientation with respect to the GB line, the periodic length L_y, and the supercell types of graphene domains are modified when the grain boundary is changed. These changes in the system symmetry lead to significant changes in the properties of the transport gap induced by the strain. In particular, differently from the data shown in Fig. 3c, the transport gap obtained for the systems in Fig. 8a and b is an asymmetric function of the strain direction (similarly as in the case presented in Fig. 6) while the gap for the system in Fig. 8c exhibits four peaks/valleys in the range of $\theta \in [-90°, 90°]$ (similarly as in the case presented in Fig. 3e). The latter feature is explained by the fact that graphene domains in the system of Fig. 8c have supercells of type 2 while the domains in other systems of Fig. 8a and b and Fig. 1c have supercells of type 1. The systems in Fig. 8d and e even exhibit a more
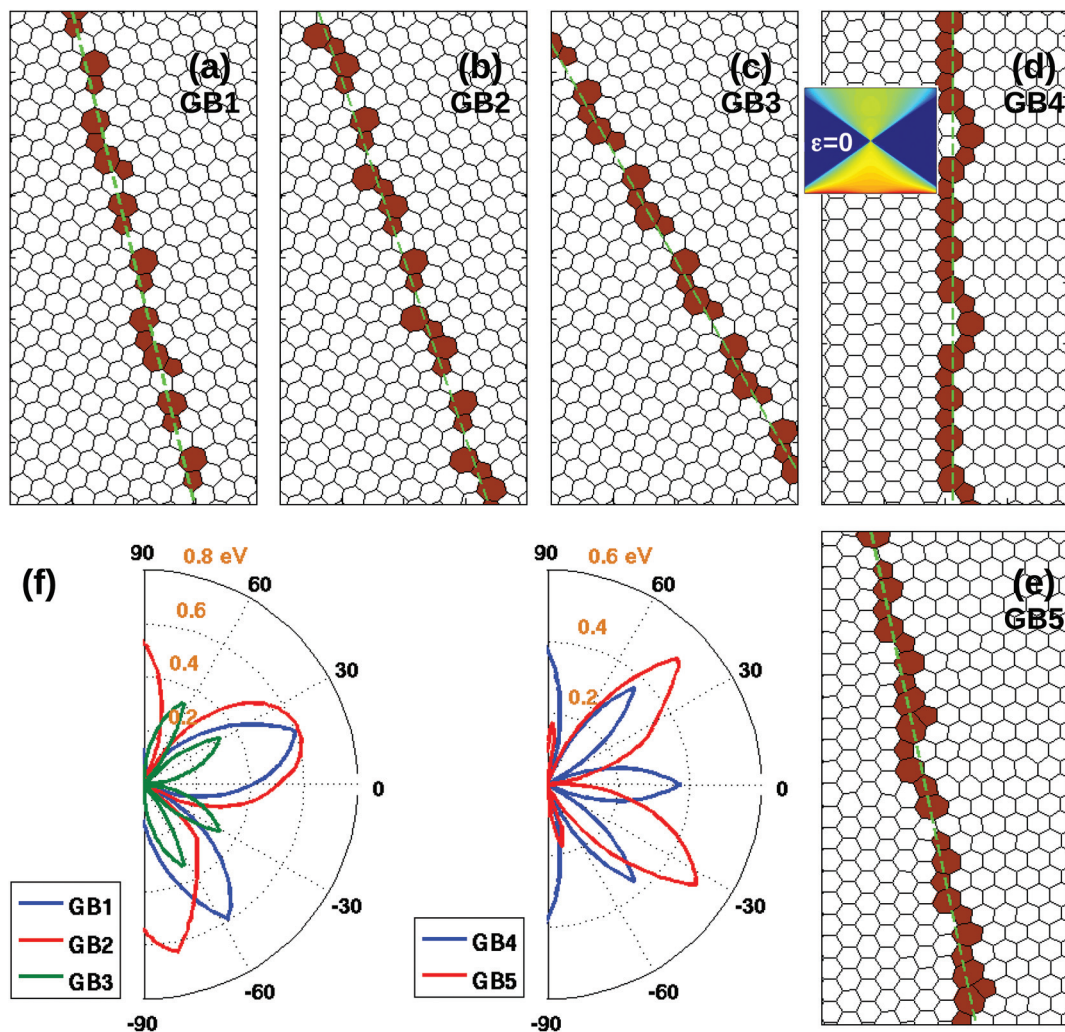
Fig. 8 (f) Polar plots of a strain-induced transport gap with respect to the strain direction obtained in five systems (a–e) while the strain magnitude ε = 5% is fixed. The inset of (d) shows the ($E - k_y$) map of transmission obtained in the corresponding system under zero strain.

significant change in the properties of the transport gap, compared to the results obtained for the system in Fig. 7a. Both changes in the periodic length L_y (Fig. 8d) and/or in the GB direction (Fig. 8e) lead to a modification of the supercell type of the two graphene domains. While they have different supercell types in Fig. 7a, these domains have the same supercell of type 2 in the systems of Fig. 8d and e. When no strain is applied, the former system behaves as a semiconducting channel while the latter ones are semimetallic, as shown for instance in the inset of Fig. 8d. Importantly, it demonstrates again that a metal–semiconductor transition induced by a strain can be achieved in all the systems studied.

Thus, our results show that generally, (i) a large generation/modulation of the transport gap by a strain can be achieved in all systems where the two graphene domains are arranged in different orientations, (ii) this gap is not only dependent on the strain (magnitude and direction) but also is very sensitive to the symmetry properties of the global system (*i.e.*, depending on the nature of the grain boundary and the orientation of

the two graphene domains). In order to provide a more complete picture about these properties, we plot in Fig. 9 the maximum of the transport gap as a function of the misorientation angle between the two graphene domains, summarizing the possibility of a strain-induced transport gap in many different systems. This maximum value of the transport gap is obtained when varying the strain direction while the strain magnitude is fixed at ε = 5%. Note that the misorientation angle is determined here as the angle between the high symmetry (armchair or zigzag) directions of the two domains and hence the full range of ϕ_{MO} is only [0°, 30°]. Indeed, besides its dependence on the misorientation angle, the transport gap exhibits a strong variation with respect to other structure parameters such as the GB direction, the periodic length L_y, the relative orientation angle of graphene domains with respect to the grain boundary, the commensurability of these two domains, *etc*. However, two common properties are observed. First, the gap tends to zero when the misorientation angle approaches zero. Second, the variation is strong for moderate
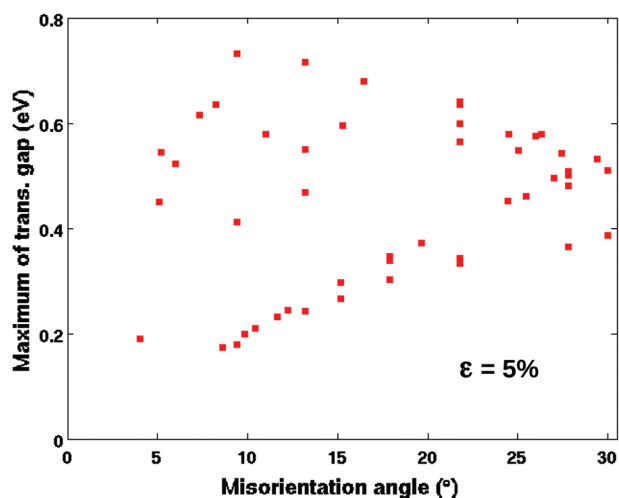
Fig. 9 Maximum of the transport gap when varying the strain direction is summarized for many different graphene GB systems as a function of the misorientation angle between the two graphene domains. The strain magnitude ε = 5% is fixed.

angles but it weakens and the transport gap tends to a finite value when the misorientation angle reaches 30°. The latter feature suggests that to obtain a finite transport gap and to avoid its strong sensitivity to the system symmetry, the systems with a misorientation angle of about 30° are good candidates. Additionally, note that the data obtained in the incommensurable systems where two domains have different supercell types are not included in Fig. 9. In such cases, the transport gap is finite even without a strain and its maximum value when a strain is applied is generally in the range of $\left[\hbar v_{\mathrm{F}} \dfrac{2\pi}{3L_y}, \hbar v_{\mathrm{F}} \dfrac{\pi}{L_y}\right]$, as already discussed above. Otherwise, the gap also has a strong sensitivity to other symmetry properties of the global system, as discussed for the data in Fig. 9.

Finally, though the transport gap is complicatedly dependent on all structure parameters (i.e., the nature of grain boundary and both orientations of the two graphene domains), we would like to demonstrate here a common property that can be simply used to estimate the transport gap in any graphene periodic GB system. As shown above in Fig. 2, the transport gap is essentially due to the mismatch of band structures of the two graphene domains and hence its value can be estimated from the width of the energy interval in which there is no overlap between their band structures along the k_y axis. On this basis, we propose a simple numerical scheme to estimate the transport gap without any expensive atomistic simulation. The transport gap can be determined by the following steps: (i) determine the supercells (with two translation vectors $L_{x,y}$) of the two graphene domains, for instance, from experimental micrographs;[61] (ii) compute the energy bands and the (conduction and valence) band edges of these domains as a function of momentum k_y using the tight binding Hamiltonian given in section II; (iii) the transport gap is finally determined as the energy interval in which the bands

of the two domains do not overlap each other (see Fig. 2). To determine the supercells of graphene domains, note that their relaxed lattices far from the defect region are, in principle, identical to that of pristine graphene. This numerical scheme is simple and could be a very useful tool for predicting and designing the GB systems with desirable properties.

B. Strain *versus* defect scattering

In polycrystalline graphene, the scattering on the GB defects is one of the important factors that strongly affects the transport properties (carrier mobility, mean free path, conductivity and so on[9–11]). In this subsection, we investigate these scattering mechanisms when a strain is applied. Our calculations have shown that the conductance of graphene is drastically affected and strongly degraded in the presence of these GB defects. As discussed in the previous subsection, a finite transport gap can open and hence the conductance is further reduced by the effects of the strain. However, we additionally found that in the systems where the two graphene domains have the supercell of type 2 as shown in Fig. 4b, e.g., the AM02 system (Fig. 1e), the strain effects have another peculiar property, i.e., they can significantly modify the GB defect scattering. In Fig. 10a, the conductance as a function of Fermi energy was calculated in the AM02 system for different applied strains and compared to the unstrained case. To avoid finite transport-gap effects, only strain directions θ = 0° and 90° are considered here, i.e., $D_{1y} \equiv D'_{2y}$ and $D_{2y} \equiv D'_{1y}$ even though $D_{1y} \neq D'_{1y}$ and $D_{2y} \neq D'_{2y}$. Instead of its reduction, the conductance around the neutrality point is found to be significantly enhanced when a strain is applied. Indeed, its value is about twice the conductance obtained in the unstrained case. When a strain is applied, the band structure of both graphene domains is deformed and the separation of Dirac cones D and D' of each domain along the k_y axis is observed, as illustrated in Fig. 10b. Interestingly, the enhancement of conductance is especially significant in the energy window $[E_1, E_2]$ where there is no overlap between the D and D' cones along the k_y axis. Beyond this energy window, the conductance enhancement weakens gradually when increasing the energy.

In order to explain this peculiar phenomenon, schematic diagrams illustrating the transmission/reflection processes, band profiles of both graphene domains, and phase difference $\Delta\phi$ between the incoming and reflected states calculated at the atomic sites are presented in Fig. 11. When transmitting through the graphene system, the incoming wave e^{ikx} is separated at the grain boundary into two components te^{ikx} and re^{-ikx} that correspond to the transmitted and reflected waves, respectively. The transmission and reflection probabilities of this process are simply determined by $T = |t|^2$ and $R = |r|^2$. If there is no scattering source (i.e., no defect), $T = 1$ and $R = 0$. The presence of defects in the GB should enhance the transition between the incoming and reflected states (i.e., should increase the amplitude of r) and hence enlarge the reflection. The transition probability of these processes is, in principle, dependent on both the nature of the defects and the properties of these two states.
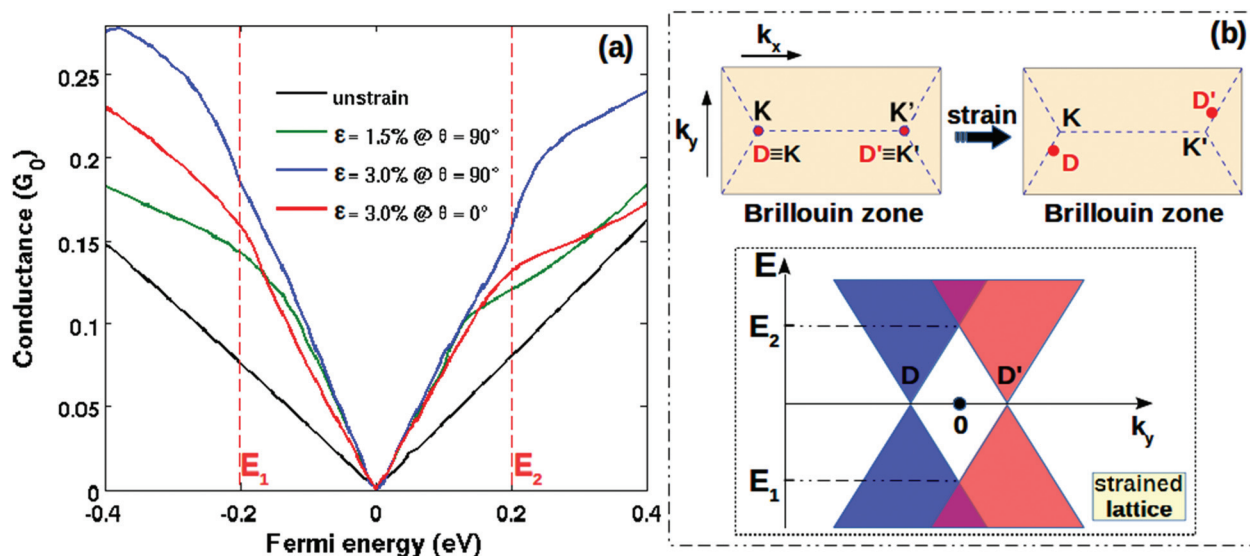
Fig. 10 (a) Zero-temperature conductance as a function of Fermi energy in the AM02 system (see Fig. 1e) for different applied strains, with $G_0 = e^2 W/h L_y$. (b) Schematics illustrating the Brillouin zone and band profiles along the k_y axis for two graphene domains when a strain is applied.
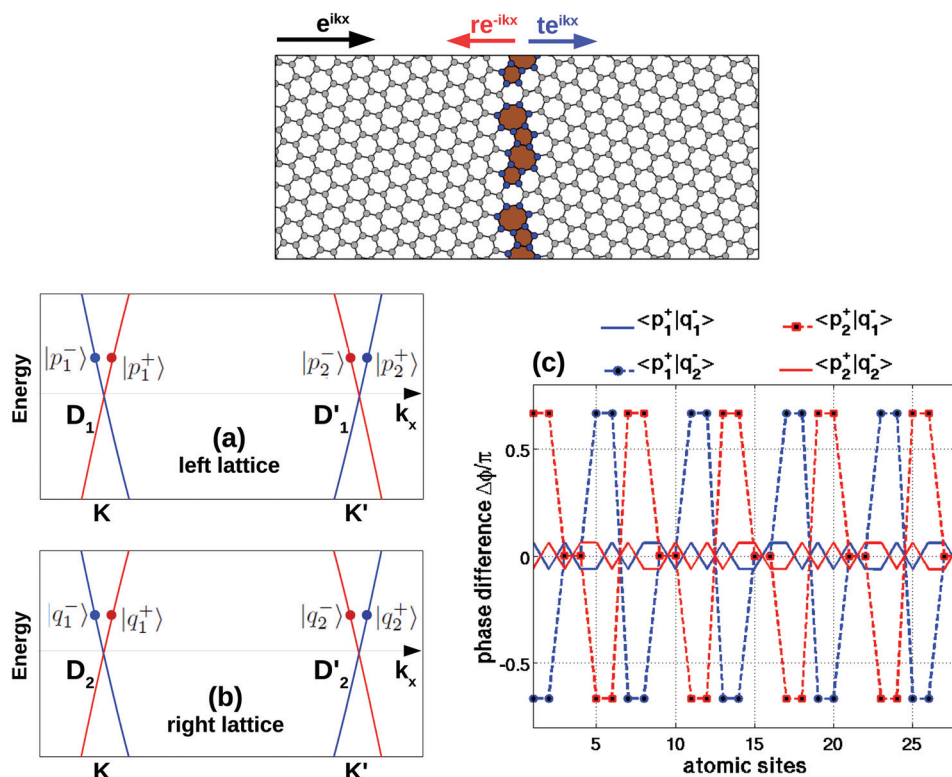

Fig. 11 The top panel illustrates transmission and reflection processes at the grain boundary. Two diagrams (a, b) depict the band profile of graphene domains along the k_x-axis. The phase difference $\Delta\phi$ between the incoming state $|p^+\rangle$ and reflected state $|q^-\rangle$ along the Oy axis is displayed in (c).

Here, we would like to remind the readers of a peculiar phenomenon in graphene: the parity symmetry of the sub-bands in zigzag graphene nanoribbons (ZGNRs).[62] Because of their inversion symmetry, the subbands of ZGNRs have alter-natively even/odd parity wavefunctions $|\psi\rangle$. These properties also imply that $|\langle\psi^K|\psi^{K'}\rangle| \simeq 0$ if these states have different parity symmetries while $|\langle\psi^K|\psi^{K'}\rangle|$ is high when they have the same parity. In ZGNR p–n junctions, the superimposed

potential acts as an intervalley scattering source. However, because of the parity symmetries only transitions between states of the same parity are allowed while they are blocked between states of different parities. This is the so-called parity selective tunneling in ZGNR devices. Interestingly, similar properties are found in the system studied here. Note that while the transition processes from the $|p^+\rangle$ states in the left domain to the states $|q^+\rangle$ in the right one contribute to the transmission, the coupling between $|p^+\rangle$ and $|q^-\rangle$ states corresponds to the reflection (see the illustration in Fig. 11). The data in Fig. 11c show that the states $|p_1^+\rangle$ and $|q_1^-\rangle$ (and similarly, the states $|p_2^+\rangle$ and $|q_2^-\rangle$) have the same symmetry property (i.e., the phase difference $\Delta\phi$ is very small) but $\Delta\phi$ between the states $|p_1^+\rangle$ and $|q_2^-\rangle$ (similarly, between $|p_2^+\rangle$ and $|q_1^-\rangle$) is large and varies strongly along the atomic position. This leads to the fact that their projection is high in the former case while it is very small in the latter one, similarly to the even/odd parity properties of subbands in the ZGNRs mentioned above. These properties suggest that the strain-induced degradation of defect scattering (i.e., the conductance enhancement) can be understood as follows. First, defect scattering tends to promote the transition between the states $|p^+\rangle$ and $|q^-\rangle$ and hence to reduce significantly the conductance of the GB systems. In the unstrained case, all four processes $|p_1^+\rangle \rightarrow |q_{1,2}^-\rangle$ and $|p_2^+ \rightarrow |q_{1,2}^-\rangle$ contribute to the reflection. When a strain is applied, the Dirac cones D and D' are separated along the k_y axis and hence the processes $|p_1^+\rangle \rightarrow |q_1^-\rangle$ and $|p_2^+\rangle \rightarrow |q_2^-\rangle$ are forbidden. Moreover, due to their symmetry properties, the transition probability of the processes $|p_1^+\rangle \rightarrow |q_1^-\rangle$ and $|p_2^+\rangle \rightarrow |q_2^-\rangle$ (i.e., between states of the same symmetry) should be much larger than that for $|p_1^+\rangle \rightarrow |q_2^-\rangle$ and $|p_2^+\rangle \rightarrow |q_1^-\rangle$ (i.e., between states of different symmetries). Consequently, the disappearance of the former processes is suggested to be the principal reason for the reduction of reflection at the GB (i.e., of the conductance enhancement) in the strained system, compared to the unstrained case. This also explains why the conductance enhancement gradually weakens at higher energies beyond the energy window $[E_1, E_2]$, when the overlap between the D and D' cones reappears as in the unstrained system. Note that because of symmetry reasons, the properties observed here do not occur in systems where the two graphene domains have the supercell of type 1 as schematized in Fig. 4c.

Together with our previous findings on the strain-induced transport gap, the results obtained here demonstrate the decisive role of the lattice symmetry in the transport picture of graphene systems, thus motivating further investigations on these graphene hetero-channels in view of using strain engineering to restrain the detrimental impact of defects on the transport properties of polycrystalline graphene devices.[9–11]

C. Suggested applications

In the previous sections, we demonstrated that (i) the transport properties of graphene GB systems are very sensitive to strain (both in magnitude and direction), (ii) strain engineering can be used to open a finite transport gap in all systems
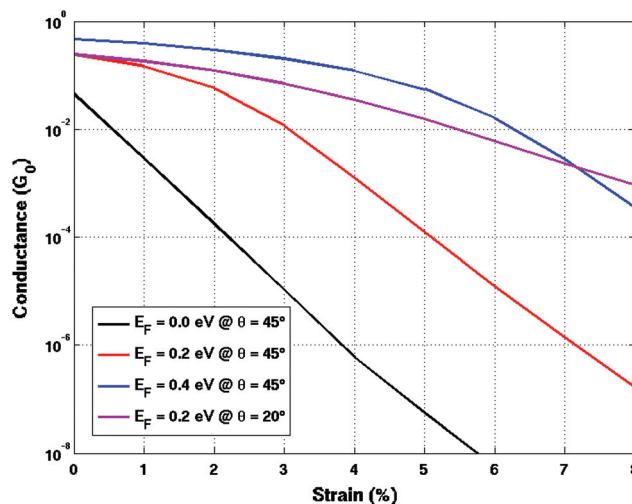

Fig. 12 Conductance in the ZZ03 system (see Fig. 1c) as a function of strain magnitude for different Fermi levels and strain directions. $G_0 = e^2 W/hL_y$. The simulations were performed at room temperature.

where the two graphene domains have different orientations and (iii) a large gap of about a few hundred meV can be achieved with a strain as small as a few percents. Unquestionably, such properties should make these graphene heterostructures very interesting for practical applications.

Room-temperature conductance of the ZZ03 system (see in Fig. 1c) as a function of strain magnitude obtained for different Fermi levels and strain directions is presented in Fig. 12. Indeed, due to its strong strain-sensitivity, the conductance can be largely modulated when varying the strain magnitude (range of a few percents) and strain direction. In particular, the conductance can be reduced by a factor of ~10^5 and 10^3 at $E_F = 0$ and 0.2 eV, respectively, for a small strain of ~4–5%. The conductance can also be significantly modulated when changing the strain direction from $\theta = 20°$ to 45° for $E_F = 0.2$ eV. This result suggests the possible use of this graphene system in highly sensitive strain nano-sensors. Given the large strain-induced gap, the system could be also very promising for application in flexible transistors. Indeed, a room-temperature ON/OFF ratio (i.e., $G_{E_F = 0.4\text{eV}}/G_{E_F = 0}$) as large as ~$10^4$–$10^5$ can be achieved when a strain of only 3–4% is applied, as shown in Fig. 12.

Besides the two applications mentioned above, this system can also be used in another electronic device, namely the p–n junction (or tunnel diode[63]), where the interband tunneling between electron states of the n-side and hole states of the p-side is the main conduction mechanism. Our proposed device, where one graphene domain is n-doped while the other one is p-doped, is schematized in Fig. 13a. The doping profile is characterized by the potential difference ΔU between two graphene domains that is additionally introduced in the tight-binding Hamiltonian given in section II. Our idea consists of considering that in this device, while the strain can lead to the separation of Dirac cones of the graphene domains along the k_y-axis, the doping is used to generate their relative shift in
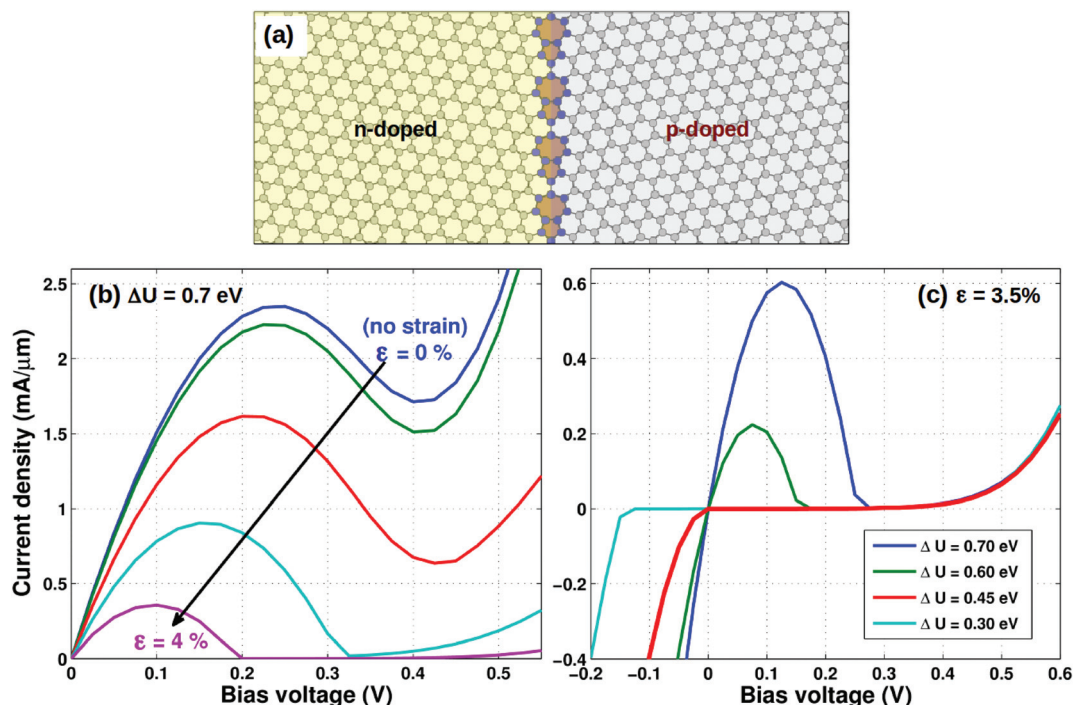
Fig. 13 Schematic of the graphene p–n junction (a) and its corresponding I–V characteristics obtained for different applied strains (b) and different doping levels ΔU (c). The strain was applied in the direction $\theta = 45°$ and all the simulations were performed at room temperature.

energy. The combination of these two features can offer the possibility of modulating the energy gap of the transmission function and hence of generating strong non-linear I–V characteristics. In Fig. 13b and c, the I–V characteristics obtained for different strains (b) and different doping levels (c) are displayed. For a fixed potential difference $\Delta U = 0.7$ eV (Fig. 13b), I–V characteristics with only a weak effect of negative differential conductance (NDC) are observed when no strain is applied. This is an expected result since the graphene system has a zero transport gap and the interband tunneling current cannot be strongly switched off. However, when a strain is applied, though the peak current is reduced, the valley current can be very strongly suppressed, leading to a very strong NDC behavior with an extremely large peak-to-valley ratio. Indeed, it can reach values as large as ~270 and 792 for strains of 3.5 and 4%, respectively. Moreover, in Fig. 13c, the I–V characteristics were calculated for different ΔU while the strain is fixed at 3.5%. In a finite range of forward bias, the current is found to be strongly modulated by varying the doping level ΔU. For an appropriate doping (i.e., $\Delta U \simeq 0.45$ eV here), the current can be totally suppressed in a finite range of forward bias. However, it still increases rapidly when applying and raising a reverse bias, implying a strong rectification effect.

To explain the mechanisms at the origin of these strong non-linear effects, $(E - k_y)$-maps of the transmission probability obtained at different biases are plotted in Fig. 14. The key ingredient consists of using the strain/doping-induced modulation of the band profile to engineer the energy gap and transmission through the graphene p–n junction. The transmission is large in the energy regions where the bands of the two graphene domains overlap, otherwise, an energy gap is achieved. At a low bias and for high doping (i.e., $\Delta U > E_g$, where E_g is the strain-induced gap obtained without doping), there are three overlapped regions (i.e., high transmission), namely, the high-energy (thermionic), middle (interband tunneling) and low-energy (thermionic) ones as shown in Fig. 14a. In the p–n junctions considered here, the transmission in the interband tunneling region contributes mostly to the current and a high peak-current is observed at a low bias. When raising the bias, the potential profile is modulated and this interband tunneling region disappears at a high bias (Fig. 14b). This leads to a large energy gap covering the energy window $[E_{FL}, E_{FR}]$ and hence the current is almost suppressed if a large enough strain is applied. Indeed, a very small valley current and a strong NDC behavior can be obtained as shown in Fig. 13. Additionally, for a given strain (i.e., a given E_g) and a doping level corresponding to $\Delta U \simeq E_g$, the transport picture is as shown in Fig. 14b if a forward bias is applied and a current gap is hence obtained in a finite range of forward bias. In contrast, when applying and raising the reverse bias, the interband tunneling region shown in Fig. 14a is extended and the current increases rapidly with the bias. This explains the strong rectification effect observed in Fig. 13b.

Thus, when considering the possibility of modulating the electronic properties of graphene using strain, the graphene GB systems appear to be very promising for applications as in strain nanosensors, flexible transistors and p–n tunnel junctions with strongly non-linear I–V characteristics.
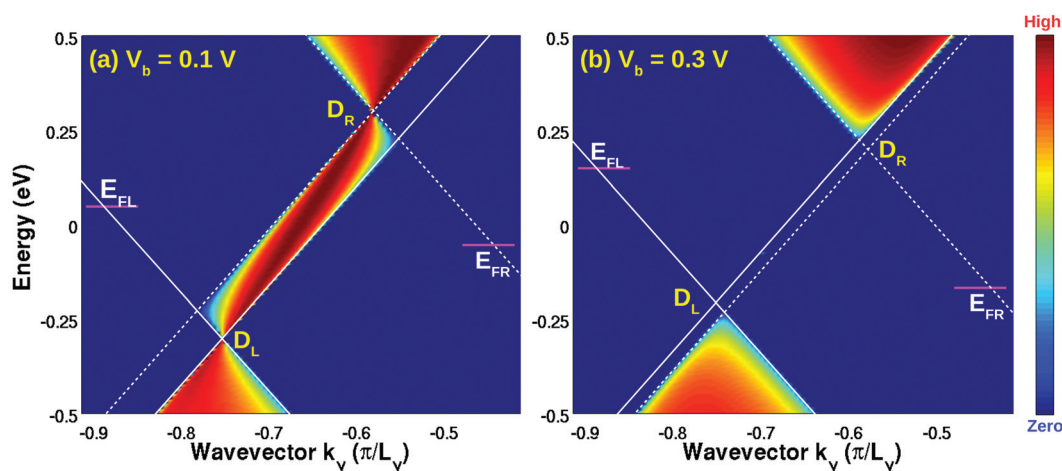
Fig. 14 $(E - k_y)$-maps of transmission probability in the graphene p–n junction of Fig. 13 for different applied biases: V_b = 0.1 V (a) and 0.3 V (b). The parameters ΔU = 0.7 eV, ε = 3.5%, and θ = 45° were considered in the calculations.

IV. Summary

By means of atomistic simulations, we have reported on a theoretical study of the electronic transport in graphene systems containing a single grain boundary and provided a systematical analysis on the effects of uniaxial strain and lattice symmetry on their electronic properties. First, it has been shown that the transport properties of these systems are not only sensitive to the magnitude of strain but also dependent on its applied direction and the lattice symmetry of the two graphene domains surrounding the boundary. On this basis, strain engineering is suggested to be used to open a finite transport gap in all systems where two graphene domains are arranged in different orientations. By choosing appropriately the strain direction, a large transport gap (*i.e.*, ~ a few hundred meV) and/or a large modulation of the gap can be achieved with a strain as small as a few percents. The dependence of this transport gap on the lattice symmetry of graphene domains (*i.e.*, their misorientation, the type and size of their supercell, their relative commensurability) has been also carefully investigated and clarified. We have additionally reported on a peculiar phenomenon concerning strain effects on the mechanisms of defect scattering in these graphene heterostructures. We have shown that in specific graphene grain boundaries where the energy bands have different parity symmetries (similarly to that in ZGNRs), strain effects can be used to reduce GB defect scattering and significantly enhance the conductance. Finally, on the basis of a large strain-induced transport gap, we suggest that the graphene systems with a single grain boundary are very promising for applications as highly sensitive strain sensors, flexible electronic devices and p–n junctions with strongly non-linear *I–V* characteristics. Hence, our study provides a good and direct guide for recent experiments (for instance, as in ref. 49 and 50) to achieve desirable transport properties with these kinds of graphene heterostructures and to exploit them in practical applications.

Finally, note that an important factor may have an influence on our results. Since our simulations are performed on periodic grain boundary structures, the presence of a disorder may have an important impact on their transport properties. In particular, the disorder can break the conservation of momentum k_y and thus can induce some leakage current within the gap region. However, it has been demonstrated in ref. 41 that this current is still low for moderate disorder in grain boundaries. More interestingly, some recent efforts to control the periodicity of grain boundaries at a large scale have been experimentally realized.[49,60,64,65] For instance, periodic grain boundaries as long as a few ten nanometers can be achieved after the thermal reconstruction of aperiodic ones.[64] These samples of reconstructed polycrystalline graphene could be very useful to check the interesting findings predicted in this work for periodic GB graphene heterostructures.

Acknowledgements

References

1 A. C. Ferrari, *et al.*, *Nanoscale*, 2015, **7**, 4598–4810.
2 Y. Zhang, L. Zhang and C. Zhou, *Acc. Chem. Res.*, 2013, **46**, 2329–2339.

3 L. P. Biró and P. Lambin, *New J. Phys.*, 2013, **15**, 035024.

4 O. V. Yazyev and Y. P. Chen, *Nat. Nanotechnol.*, 2014, **9**, 755–767.

5 A. W. Cummings, *et al.*, *Adv. Mater.*, 2014, **26**, 5079–5094.

6 Y. Wei, J. Wu, H. Yin, X. Shi, R. Yang and M. Dresselhaus, *Nat. Mater.*, 2012, **11**, 759–763.

7 H. I. Rasool, C. Ophus, W. S. Klug, A. Zettl and J. K. Gimzewski, *Nat. Commun.*, 2013, **4**, 2811.

8 Y. I. Jhon, P. S. Chung, R. Smith, K. S. Min, G. Y. Yeom and M. S. Jhon, *RSC Adv.*, 2013, **3**, 9897.

9 H. S. Song, S. L. Li, H. Miyazaki, S. Sato, K. Hayashi, A. Yamada, N. Yokoyama and K. Tsukagoshi, *Sci. Rep.*, 2012, **2**, 337.

10 D. V. Tuan, J. Kotakoski, T. Louvet, F. Ortmann, J. C. Meyer and S. Roche, *Nano Lett.*, 2013, **13**, 1730–1735.

11 D. Jiménez, *et al.*, *Appl. Phys. Lett.*, 2014, **104**, 043509.

12 Z. Fei, *et al.*, *Nat. Nanotechnol.*, 2013, **8**, 821–825.

13 A. A. Balandin, *Nat. Mater.*, 2011, **10**, 569–581.

14 Y. Lu and J. Guo, *Appl. Phys. Lett.*, 2012, **101**, 043112.

15 A. Y. Serov, Z.-Y. Ong and E. Pop, *Appl. Phys. Lett.*, 2013, **102**, 033104.

16 A. W. Cummings, A. Cresti and S. Roche, *Phys. Rev. B: Condens. Matter*, 2014, **90**, 161401(R).

17 O. V. Yazyev and S. G. Louie, *Phys. Rev. B: Condens. Matter*, 2010, **81**, 195420.

18 S. Dutta and K. Wakabayashi, *Sci. Rep.*, 2015, **5**, 11744.

19 F. Schwierz, *Nat. Nanotechnol.*, 2010, **5**, 487–496.

20 M. Y. Han, B. Özyilmaz, Y. Zhang and P. Kim, *Phys. Rev. Lett.*, 2007, **98**, 206805.

21 N. Kharche and S. K. Nayak, *Nano Lett.*, 2011, **11**, 5274–5278; S. Tang, *et al.*, *Sci. Rep.*, 2013, **3**, 2666.

22 A. Lherbier, *et al.*, *Nano Lett.*, 2013, **13**, 14461450; A. Zabet-Khosousi, *et al.*, *J. Am. Chem. Soc.*, 2014, **136**, 1391–1397.

23 Y. Zhang, *et al.*, *Nature*, 2009, **459**, 820–823.

24 J. Bai, X. Zhong, S. Jiang, Y. Huang and X. Duan, *Nat. Nanotechnol.*, 2010, **5**, 190–194.

25 G. Fiori, A. Betti, S. Bruzzone and G. Iannaccone, *ACS Nano*, 2012, **6**, 2642–2648.

26 L. Britnell, *et al.*, *Science*, 2012, **335**, 947–950.

27 M. Chung Nguyen, V. Hung Nguyen, H. Viet Nguyen and P. Dollfus, *Semicond. Sci. Technol.*, 2014, **29**, 115024.

28 V. Hung Nguyen, H. Viet Nguyen, J. Saint-Martin and P. Dollfus, *Nanotechnol.*, 2015, **26**, 115201.

29 V. Hung Nguyen and P. Dollfus, *J. Phys. D: Appl. Phys.*, 2016, **49**, 045306.

30 Y. Wang, *et al.*, *Adv. Funct. Mater.*, 2015, **25**, 68–77.

31 K. S. Kim, *et al.*, *Nature*, 2009, **457**, 706–710.

32 B. K. Sharma and J.-H. Ahn, *Solid-State Electron.*, 2013, **89**, 177–188.

33 V. M. Pereira, A. H. Castro Neto and N. M. R. Peres, *Phys. Rev. B: Condens. Matter*, 2009, **80**, 045401.

34 V. M. Pereira and A. H. Castro Neto, *Phys. Rev. Lett.*, 2009, **103**, 046801.

35 N. Levy, *et al.*, *Science*, 2010, **329**, 544–547.

36 V. M. Pereira, *et al.*, *Europhys. Lett.*, 2010, **92**, 67001.

37 G.-X. Ni, *et al.*, *Adv. Mater.*, 2014, **26**, 1081.

38 F. Guinea, M. I. Katsnelson and A. K. Geim, *Nat. Phys.*, 2010, **6**, 30–33.

39 T. Low and F. Guinea, *Nano Lett.*, 2010, **10**, 3551.

40 F. Zhai and L. Yang, *Appl. Phys. Lett.*, 2011, **98**, 062101.

41 O. V. Yazyev and S. G. Louie, *Nat. Mater.*, 2010, **9**, 806–809.

42 S. Bala Kumar and J. Guo, *Nano Lett.*, 2012, **12**, 1362–1366.

43 P. Y. Huang, *et al.*, *Nature*, 2011, **469**, 389–392.

44 J. Kotakoski and J. C. Meyer, *Phys. Rev. B: Condens. Matter*, 2012, **85**, 195447.

45 G.-H. Lee, *et al.*, *Science*, 2013, **340**, 1073–1076.

46 G. Jung, Z. Qin and M. J. Buehler, *Extreme Mech. Lett.*, 2015, **2**, 52–59.

47 A. Shekhawat and R. O. Ritchie, *Nat. Commun.*, 2016, **7**, 10546.

48 H. H. P. Garza, *et al.*, *Nano Lett.*, 2014, **14**, 4107–4113.

49 Q. Yu, *et al.*, *Nat. Mater.*, 2011, **10**, 443–449.

50 A. W. Tsen, *et al.*, *Science*, 2012, **336**, 1143–1146; P. Yasaei, *et al.*, *Nat. Commun.*, 2014, **5**, 4911; V. Kochat, *et al.*, *Nano Lett.*, 2016, **16**, 562–567.

51 L. Lindsay and D. A. Broido, *Phys. Rev. B: Condens. Matter*, 2010, **81**, 205441.

52 S. Chen, *et al.*, *Nat. Mater.*, 2012, **11**, 203–207.

53 H. Zhang, Z. Duan, X. Zhang, C. Liu, J. Zhang and J. Zhao, *Phys. Chem. Chem. Phys.*, 2013, **15**, 11794.

54 X. Xu, *et al.*, *Nat. Commun.*, 2014, **5**, 3689.

55 P. Vancsó, *et al.*, *Appl. Surf. Sci.*, 2014, **291**, 58–63.

56 E. N. Koukaras, G. Kalosakas, C. Galiotis and K. Papagelis, *Sci. Rep.*, 2015, **5**, 12923.

57 J.-W. Liang, *et al.*, *J. Phys.: Condens. Matter*, 2015, **27**, 083001.

58 O. L. Blakslee, D. G. Proctor, E. J. Seldin, G. B. Spence and T. Weng, *J. Appl. Phys.*, 1970, **41**, 3373.

59 M. P. Anantram, M. S. Lundstrom and D. E. Nikonov, *Proc. IEEE*, 2008, **96**, 1511–1550.

60 J.-H. Chen, *et al.*, *Phys. Rev. B: Condens. Matter*, 2014, **89**, 121407(R).

61 C. Ophus, A. Shekhawat, H. Rasool and A. Zettl, *Phys. Rev. B: Condens. Matter*, 2015, **92**, 205402.

62 A. Cresti, G. Grosso and G. P. Parravicini, *Phys. Rev. B: Condens. Matter*, 2008, **77**, 233402.

63 A. Seabaugh and R. Lake, Tunnel diodes, in *Encyclop. Appl. Phys.*, Am. Inst. Phys. VCH Pub., NY, 1998, vol. 22, pp. 335–359.

64 B. Yang, H. Xu, J. Lu and K. P. Loh, *J. Am. Chem. Soc.*, 2014, **136**, 12041–12046.

65 V. Luan Nguyen and Y. Hee Lee, *Small*, 2015, **11**, 3512–3528.